Delft University of Technology

A method for segmentation of pebble images in the presence of shadows

Cattapan, Alessandro; Gurini, Alessia; Paron, Paolo; Ballio, Francesco; Franca, Mário J.

Important note
To cite this publication, please use the final published version (if applicable).
Please check the document version above.

RESEARCH ARTICLE

ESPL **WILEY**

A method for segmentation of pebble images in the presence of shadows

Alessandro Cattapan[1,2] 🔘 | Alessia Gurini[1,3] | Paolo Paron[1] | Francesco Ballio[3] |
Mário J. Franca[4] 🔘

[1]IHE Delft, Institute for Water Education, Delft, The Netherlands

[2]Department of Hydraulic Engineering, Delft University of Technology, Delft, The Netherlands

[3]Civil and Environmental Engineering Department, Politecnico di Milano, Milan, Italy

[4]Institute for Water and River Basin Management, Karlsruhe Institute of Technology, Karlsruhe, Germany

Correspondence
Alessandro Cattapan, Department of Hydraulic Engineering, Delft University of Technology, Stevinweg 1,2628 CN, Delft, The Netherlands.
Email: a.cattapan@tudelft.nl

Abstract

The quantification of pebble shape has been of interest to geomorphologists for decades. Several authors developed parameters to describe pebble shapes from their images. The extraction of this information from images involves two steps: the segmentation of pebble contours and the application of a computational geometry algorithm to estimate shape parameters. When images are taken in the field, unavoidable shadows might hinder the possibility of using automatic segmentation methods. This paper introduces a new method for automatic segmentation of pebbles that improves segmentation accuracy in the presence of shadows. The method is based on the Canny edge detection algorithm which uses a double thresholding process to provide a classification of the strength of the detected edges. The proposed method applies this algorithm with an ensemble of thresholding values, estimating, for each pixel, the probability of being an edge. The resulting pebble contours were analysed using two computational geometry algorithms to obtain shape parameters. The algorithm was calibrated on a sample of five pebbles and then validated on a sample of 1696 pebbles. Its accuracy has been estimated by comparing the resulting shape parameters with those obtained using reference software, which was used as ground truth (GT). The proposed segmentation method was capable of accurately segmenting around 91% of the sample with a relative error for roundness of -1.7% and -0.4%; for elongation of -0.2% and -0.3% and for circularity of 0.2% and 0.1%, when shape parameters were computed using the algorithms of Zheng or Roussillon, respectively. The method could therefore be used to segment images of pebbles collected in the field with low contrast and shadowing, providing comparable accuracy with 'manual' segmentation, while removing operator bias.

KEYWORDS
computational geometry, image processing, sediment morphometry, segmentation, shadow effect

1 | INTRODUCTION

The detailed description of sediment transport processes in rivers is still hindered by technological measurement limitations (Cassel, Dépret, & Piégay, 2017; Cassel, Piégay, & Lavé, 2017; Rickenmann, 2017; Schneider et al., 2016; Wyss et al., 2016). Historically, sediment transport rates have been considered to depend on pebbles' mass, almost invariably expressed by a linear measure representative of their size and by their density (Engelund & Hansen, 1967; Meyer-Peter & Müller, 1948; van Rijn, 1984). Recently, the impact of pebble shape on transport rates was also acknowledged (Cassel et al., 2021; Deal et al., 2023). Changes in sediment size and shape as a function of their transport history within a river basin have been observed in the field and studied empirically, analytically and

numerically for decades. These changes have been attributed to the combination of a series of processes: attrition (Attal & Lavé, 2009; Kodama, 1994; Krumbein, 1941; Lewin & Brewer, 2002; Wentworth, 1919), selective transport (Bradley, Fahnestock, & Rowekamp, 1972; Dawson, 1988; Seal & Paola, 1995; Ferguson et al.,1996) and physical and chemical weathering (Bradley, 1970; Jones & Humphrey,1997). Some authors also suggested the possibility of 'in-place abrasion' (Brewer, Leeks, & Lewin, 1992; Schumm & Stevens, 1973), which is the process of sediment deterioration owing to vibrations that pebbles are subject to because of fluctuations of lift and drag forces.

Two of the most widespread technologies providing quantitative data on sediment size and shape are laser scanning and image-based techniques. Both techniques have been applied either on untouched samples in the field (Adams, 1979; Butler, Lane, & Chandler, 2001; Chang & Chung, 2012; Hodge, Brasington, & Richards, 2009; Huang, Atkinson, & Wang, 2018; Wang et al., 2013; Warrick et al., 2009) or on pebbles collected and later analysed under controlled conditions and by applying several methods (Cassel et al., 2018; Hayakawa & Oguchi, 2005). In general, image-based methods represent a cheaper solution, especially if the analysis is limited to pebbles size, whose accurate estimation can be achieved even with lower-resolution images (Detert & Weitbrecht, 2012; Roussillon et al., 2009; Zheng & Hryciw, 2015). In this case, the grain size distribution of the surficial material can also be estimated using images collected by Unmanned Aerial Vehicles (UAV) (Carbonneau, Bizzi, & Marchetti, 2018; Carbonneau, Lane, & Bergeron, 2004; Langhammer et al., 2017; Woodget & Austrums, 2017). This method allows the acquisition of a large number of pebbles in a relatively short time; however, pebbles' imbrication and coverage by vegetation and soil material limit its applicability to shape estimation. Furthermore, while mean grain size can be inferred from the spectral decomposition of images of exposed sediment deposits (Buscombe, Rubin, & Warrick, 2010), a similar approach has not yet proven applicable for shape estimation. Several algorithms were proposed to allow the segmentation of contacting and overlapping objects, both in 2D and 3D settings (Koh et al., 2007; Sun, Zheng, & Li, 2019; Zheng & Hryciw, 2016), but their effect on the accuracy of shape estimates is still unclear. For these reasons, accurate estimates of sediment shape still mostly rely on the analysis of samples collected in the field and analysed under controlled conditions.

During field surveys, sediment images are often taken by placing the sampled pebbles against a flat surface capable of providing a uniform colour background (Cassel et al., 2018; Roussillon et al., 2009; Tunwal, Mulchrone, & Meere, 2020; Vangla, Roy, & Gali, 2017). Field conditions do not always allow shadow elimination, which affects image segmentation (Figure 1a). Shadow elimination is a classic problem in image analysis and computer vision which therefore produced a vast literature (Al-Najdawi et al., 2012; Ecins, Fermüller, & Aloimonos, 2014; Le & Samaras, 2020; McCallister & Hung, 2003). These methods do not find application to sediment pebble analysis, mostly because of their high variability in hue and texture, and the lack of controlled lightness conditions that can be achieved in the field. Under more controlled conditions, the geometric projection of pebbles' shadows has been used to infer their third dimension (Montenegro Ríos et al., 2013). This method requires a background capable of producing a strong hue difference to the target pebbles. Unfortunately, although many silicate and carbonate rocks present a higher intensity in the red and blue spectrum, some rocks also show relevant intensity in the green hue (e.g. rocks rich in olivine, serpentine or chlorite minerals). This makes the data acquisition process complex in the field because one should use different backgrounds for pebbles of different hues.

This manuscript proposes a new method to segment the 2D contour of pebbles from sediment images in the presence of shadows. The method is based on a probabilistic application of the Canny edge detection algorithm (Canny, 1986) and uses greyscale images; therefore, it does not require the selection of a specific background colour. Its application shows that this new method allows an accurate assessment of sediment shape properties from images collected in the
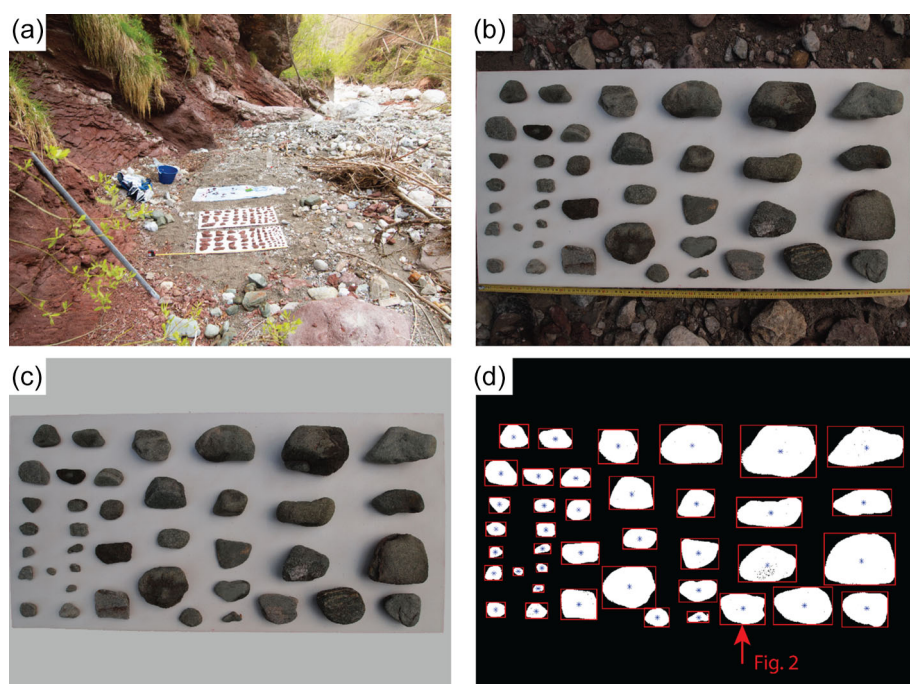
FIGURE 1 (a) Example of the field survey process. (b). JPG image of a sample of pebbles of mixed lithology collected on the Sarzana River, Italy in 2019. This image is 4032 × 3024 pixels, with a resolution of 300 dpi and a spatial resolution of around 0.26 mm/px.
(c) Image resulting after the elimination of the material outside of the whiteboard.
(d) Example of rough segmentation with the indication of centroids and bounding boxes for each pebble.

field using relatively inexpensive equipment. The model is written in MATLAB™, The MathWorks, Inc. and is available at https://github.com/ACattapan/Probabilistic-Canny-Segmentation.

2 | METHODS

2.1 | Segmentation method

Sediment images collected in the field are generally characterised by irregular shadowing and by intra-granular variations in texture and colour (Figure 1b). Because shadows reduce the local contrast near the edge of a pebble, common methods for edge detection, loosely based on intensity gradients, might not provide an accurate segmentation, for example, Canny edge detector (Canny, 1986), Sobel operator (Sobel, 2014) and Watershed algorithm (Zheng & Hryciw, 2016). The proposed method comprises two phases. Phase 1 consists of a pre-processing of the input image where the model identifies the background board on which target pebbles are placed to exclude undesired objects and roughly identifies each pebble, which will then be analysed individually. Phase 2 consists of the application of the proposed method on each pebble. The proposed method is based on the iterative application of the Canny edge detection algorithm with variable thresholding values. For each set of these values, an image of edges, variable strength, is produced. These images are then averaged to calculate the relative frequency with which each pixel has been identified as an edge, hence the probabilistic nature of the method. This probabilistic approach improves the performances of the classical Canny algorithm by allowing taking into account additional criteria for the definition of the outline of a pebble, on top of the local contrast. The detailed method will be explained in Section 2.3.

2.2 | Phase 1: image pre-processing

The first phase of the model aims at removing from the initial image areas of non-interest (Figure 1b). For this purpose, the true-colour image is first transformed into greyscale. Given the sharp change in colour and texture between the outer material and the background board, the board's edge represents a discontinuity in the light intensity, that is, these points are characterised by a significant gradient in greyscale. The image is therefore initially enhanced, increasing the contrast between the background board and the material present on the background. The contrast enhancement increases the probability that the maximum absolute value of the intensity gradient will be placed on the edges of the background board. The intensity gradient is computed by the convolution of the Sobel operator (Sobel, 2014) and the contrast-enhanced image. The background board segmentation method searches for the edges in the vertical and horizontal directions separately and proceeds sequentially by column and row, respectively. As an example, the process for the identification of the top horizontal edge is explained below; the identification of the other edges will follow an analogue process.

Assume the enhanced image to be a N by M pixels matrix. Each pixel is identified by its row and column indices, i and j, respectively. The search for the pixels composing the top horizontal edge of the background board starts from the top left of the image (row $i = 1$ and column $j = 1$) and proceeds by column. The code searches for the pixel with the highest positive gradient in the vertical direction along the column j and evaluates the following conditions:

1. When the image includes external material that encircles the background board, then the horizontal edge might not lay on column j. In this case, none of the pixels in column j have a positive gradient so the code moves to the first row of column $j + 1$.
2. If the highest positive gradient is found on pixel (i^*,j), which is located in the upper half of the image ($i^* \leq N/2$) and no previous pixel had been identified as an edge, then (i^*,j) becomes the first pixel of the horizontal edge. If other pixels had already been identified as part of the edge, the code computes the distance from the pixel identified as an edge in column $j - 1$. If this distance is smaller than 10 pixels, then the pixel (i^*,j) will also be classified as part of the horizontal edge. Hence, all pixels of column j located on rows $(i < i^*)$ will be assigned a value of 0, and all pixels on rows $(i \geq i^*)$ will be assigned a value of 1. The code will then move to the first row of column $j + 1$.
3. If the highest positive gradient is found on pixel (i^*,j) and this is located in the lower half of the image ($i^* > N/2$) or at a distance higher than 10 pixels from the pixel identified as an edge in column $j - 1$, this means that the top edge along column j is not characterised by the maximum gradient. This can be because of the presence of pebbles inside the board that produce a stronger contrast with the board itself. The upper edge along column j is therefore approximated by the pixel located on the same row as the edge pixel of column $j - 1$, and the analysis will move to column $j + 1$. This implies that the board edge is assumed to be parallel to the edge of the image.

The result is a binary mask splitting the image in two: all pixels above the top horizontal edge will have a value of 0, while all pixels on the edge and below will have a value of 1. A similar process is repeated to identify the three remaining edges. The final four binary masks are then overlapped, resulting in a binary mask where all pixels belonging to the background whiteboard have a value of 1 (Figure 1c).

This mask is then applied to the original RGB image so that the output is a true-colour representation of the whiteboard and the pebbles positioned on top of it. The outer material in the area of non-interest is replaced by a uniformly coloured region. To reduce the contrast, the colour of the outer region can be selected to be as similar as possible to the colour of the background board (Figure 1c).

Because the next phase of the model involves the analysis of each pebble individually, the image obtained at this point is converted to black and white and enhanced. Because the contrast between the whiteboard and the pebbles is generally high, their outline can be roughly identified and labelled as a separate eight-connected component. The (eight) connection is defined according to this criterion: a pixel a is eight-connected to a pixel b if b is located in a 3×3 square window surrounding pixel a, which is therefore composed of eight pixels plus pixel a itself. Each component represents the set of pixels that have been assigned a value of 1 in the black-and-white image. Comparing Figure 1c and d, it is possible to notice that, because of the presence of shadows and colour and texture changes on the surface of some pebbles, this rough segmentation can be quite inaccurate, often leading to the overestimation of the pebbles' outline. The

model builds a bounding box around each connected component, which will be the area of focus for the second phase.

2.3 | Phase 2: probabilistic Canny segmentation method

In order to assure the quality of the segmentation, and immediately remove poorly segmented pebbles, the model considers one pebble at a time which can be thought of as a two-step process.

The first step is based on the Canny edge detection algorithm (Canny, 1986; Gonzalez, Woods, & Eddins, 2009), which is widely used in image segmentation and incorporated in MATLAB™. A general overview of the method is given here, while a detailed explanation can be found in the literature (Canny, 1986; Gonzalez, Woods, & Eddins, 2009). The method is usually applied on a greyscale image, which is initially smoothed by a convolution with a Gaussian function with a given standard deviation (σ_C) and a 16×16 pixels support. The magnitude and direction of the local gradient of the smoothed image are then computed for each pixel. The underlying hypothesis is that pixels belonging to an edge should be characterised by a local maximum of the gradient in the direction of the gradient. Nonetheless, the gradient magnitude image is generally characterised by the presence of wide ridges instead of sharp edges. The algorithm, therefore, proceeds with a non-maximum suppression step: if the value of the gradient in a certain pixel is the maximum among the ones located along the gradient direction, its value is maintained, otherwise, it is suppressed that is, replaced by zero. This step produces a non-maximum suppressed gradient image which may contain false-positive and false-negative edges. The selection of the important ones for the segmentation of the objects is performed by a hysteresis thresholding process. Edges can be classified according to the 'strength', that is, the magnitude of the gradient. The algorithm defines two thresholds for the gradient magnitude: a higher threshold (C_h) and a lower one (C_l). All pixels with a gradient magnitude higher than C_h are defined as 'strong' and are automatically kept as edges. All pixels with a gradient magnitude lower than C_l are automatically discarded, while pixels with a gradient magnitude between C_h and C_l are defined as 'weak' and are kept only if they are connected to a 'strong' edge. Overall, the Canny edge detection algorithm requires the definition of three parameters: the standard deviation of the Gaussian filter (σ_C) and two thresholds C_h and C_l for edges' strength. The model first applies the algorithm using the default values for all the parameters: $\sigma_C = \sqrt{2}$, while C_h and C_l are defined in terms of percentage of the gradient magnitude values, $C_l = 0.28$ and $C_h = 0.70$.

When applied to images of sediment collected in the field, for example, Figure 1a, this method might categorise as edges not only a pebble's contour but also internal discontinuities because of variations in colour or texture (Figure 2). The presence of significant shadows might also worsen the quality of the segmentation because the maximum gradient might happen along the shadow, resulting in artificial edges not associated with the shape of the physical object (Figure 2). To assess whether the default application of the Canny algorithm successfully segmented the whole outline of a pebble, the edges resulting from its application are first classified as eight-connected components and the longest connected component is identified.
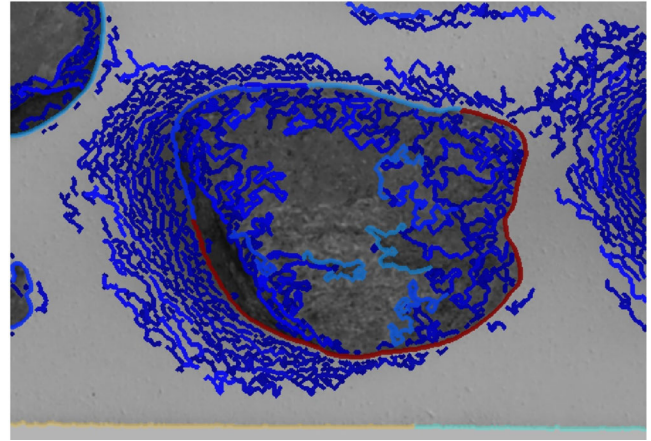

FIGURE 2 Connected components resulting from the application of the classical Canny segmentation algorithm. The red contour represents the longest connected component. Notice that, in the area where a shadow is present, on the left of the pebble, the algorithm identifies a series of possible edges, each with a different 'strength' and length.

In the absence of shadows and internal colour or texture changes, the outer border is characterised by a strong contrast with the background, and therefore, the longest connected component properly approximates the pebble's outline. In this case, the longest connected component will be a closed path; the segmentation process will stop and the model will print an image of the original pebble superimposed by the longest connected component to allow the operator to assess the quality of the segmentation and decide whether to keep the outline for further shape analysis or discard it due to an insufficient accuracy. However, in case of strong shadows or colour variations, the longest connected component properly identifies only the part of a pebble's outline facing the light source, where the image contrast is higher, for example, the red outline in Figure 2. In this case, the longest connected component will be an open path, characterised by two endpoints. The process will therefore continue with the Probabilistic Canny segmentation method which represents the second step of Phase 2.

The second step of Phase 2 is based on the hypothesis that the composite statistics of multiple applications of the Canny algorithm with different parameterisations will reveal the most significant edges, that is, the ones which are identified more frequently. The parameters that the model varies to assess the relative frequency with which edges are detected are the standard deviation of the Gaussian filter and the lower and upper thresholds on edges' strength. Parameters are selected from independent uniform distributions (see also Section 2.4). Each combination of these three parameters produces a binary image of edges. The relative frequency f with which each pixel is identified as an edge can therefore be computed. The output representation is a greyscale image, where pixels with a higher probability of being edges appear of lighter colour (Figure 3). The model then starts from one endpoint of the previously computed longest connected component and uses the edge frequency map to select new pixels to attach to eventually close the pebble's outline. The algorithm uses a square search window of size l pixels placed around each endpoint of the longest connected component (Figure 3). The selection of which pixels to attach to the actual longest connected component is

FIGURE 3 Scheme representing the variables used by the pebble segmentation model. *O* is the centroid of the connected component, and *x* is the horizontal axis. *E₁* and *E₂* are the two endpoints of the longest connected component, *α* is the angle of the first endpoint with respect to the horizontal axis, while *δ* is the angle between the endpoints. d_{C-P} is the distance between the centroid and a generic pixel within the search window (see particular A)), which has a size *l*. Finally, d_{E-P} is the distance between an endpoint and a generic pixel within the search window.
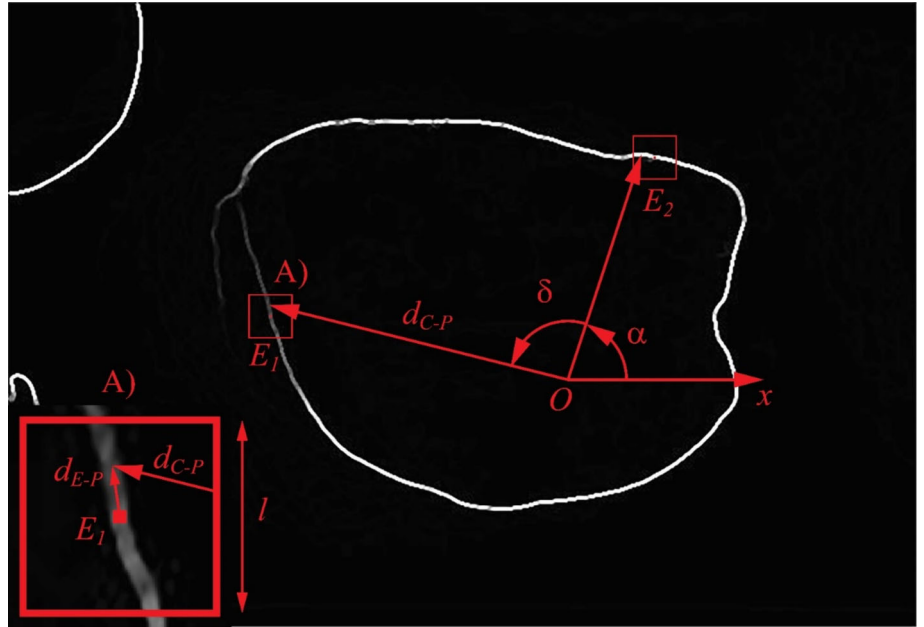
based on two assumptions. The first assumption is that pixels that have been more frequently identified as edges have a higher likelihood of being true edges. The second assumption is that pebbles tend to be overall convex; therefore, true edges should contribute to closing the pebble outline.

To implement these assumptions, the pixels' relative position must be defined. The model uses a polar coordinate system centred on the centroid of the actual longest component. The position of each pixel within the search window is therefore defined by its distance from the centre d_{C-P} and by its angle α (Figure 3). δ is the angle formed between a pixel in the search window and the opposite endpoint. d_{E-P} is the distance between a pixel in the search window and the endpoint at the centre of the window. ∇f is the gradient of the frequency map computed between each pixel in the search window and the actual endpoint. Δ is the angular distance between the current endpoints. Pixels within the search window are initially filtered according to three conditions:

$$f > 0 \tag{1}$$

$$d_{E-P} > 0 \tag{2}$$

$$\delta < \Delta \tag{3}$$

The first condition (Equation 1) filters out all pixels that were never identified as edges because their frequency *f* is lower or equal to zero. The second condition (Equation 2) filters out the current end-point by imposing that the distance of the selected pixel from the cen-tre of the search window should be positive ($d_{E-P} > 0$). The third condition (Equation 3) states that the selected pixel should contribute to the decrease of the angular distance between the endpoints ($\delta < \Delta$), in agreement with the second assumption. The first and second condi-tions must always be met while, if any pixel within the search window satisfies the third condition, the model selects the pixel with the mini-mum value of δ (even if $\delta > \Delta$). This allows the identification of locally non-convex edges. Multiple pixels may fulfil all three conditions. In this case, the model will select the new endpoint according to a list of

conditions, where each further condition is assessed only if multiple pixels meet the previous one. The list of conditions is

$$\max(\nabla f) \tag{4}$$

$$\min(d_{E-P}) \tag{5}$$

$$\min(\delta) \tag{6}$$

The meaning of these criteria is that the new endpoint is selected based on the maximum gradient of the probability for it of being an edge (Equation 4); its distance from the current endpoint should be the minimum to guarantee the continuity of the object's outline (Equation 5); and its position should be such that the angle between current endpoints will decrease (Equation 6). The pixel resulting from such selection will become the new endpoint and, should it not be adjacent to the actual centre of the search window, it will be connected to the current endpoint with a linear interpolation.

At this point, the model moves to the opposite endpoint and the process is repeated. The angular distance between endpoints iteratively decreases bringing them closer together alternatively from both sides. This process stops either if it is not possible to identify additional edges, or if the position of the endpoints is such that one of the two following conditions is met:

$$\Delta < \Delta_{thr} \tag{7}$$

$$d_{E-E} < \frac{l}{2}\sqrt{2} \tag{8}$$

The first condition (Equation 7) states that the angular distance between the endpoints is smaller than a certain threshold Δ_{thr} ($6°$ in this application). The second condition (Equation 8) states that the lin-ear distance between endpoints is smaller than half of the diagonal of the search window. At this moment, the two endpoints are connected by a straight line that closes the pebble's outline. At the end of the segmentation process, the identified contour is plotted on top of the

FIGURE 4 Outline of a pebble obtained from the application of the proposed method after calibration.

true colour image to allow a visual assessment of the quality of the result (Figure 4). The method was capable of properly segmenting the pebble (Figure 4), despite the presence of a shadow; the application of the classical Canny algorithm would have produced a set of possible edges in the area on the left of the pebble (Figure 4).

2.4 | Application area and data collection

The data used for calibrating and validating the proposed method were collected in the Sarzana River basin: a 25 km^2 alpine basin in Norh-East Italy (Figure 5). The Sarzana River is a tributary of the Cordevole River, which joins the Piave River around 31 km downstream of the Sarzana confluence. The Sarzana catchment is characterised by an alpine climate, with cold winters and temperate summers. The average annual precipitation measured at the nearby ARPAV station of Col di Prà (https://www.arpa.veneto.it/dati-ambientali/open-data/clima) over the period 2000–2021 is about 1620 mm (Brenna & Surian, 2023). The Sarzana River drains the Southeast face of the Agner Mountain group while its right-hand side is bounded by the Armarolo Mount. The elevation varies between about 2872 and 563 m above sea level.

Sediment samples ranging between fine gravel and cobbles have been collected from 11 locations, from outcrops, first-order tributaries and along the main river. Individual sediment particles have been collected, washed to remove loose soil and vegetation, dried with a cloth to avoid sparkles and placed on a 0.5 m by 1.0 m rectangular white wood board that was used as a background. Sediments were placed on the background board following two criteria: their orientation was such that the projected area on the board was maximum and their relative distance was big enough to avoid overlaps of their edges when seen from the point of view of the camera. In the current manuscript, the first criterion was applied to ensure that the maximum projected area was captured, providing reliable measures of both maximum and intermediate axes (a and b respectively).

Images were taken using an Olympus® E-PL1 digital camera, whose lens was placed as parallel as possible to the background board to limit tangential distortion. The background board and the sampled

particles were carefully placed within the edges of the image to limit radial distortion. For these reasons, images were not corrected for distortion before the analysis. A metal ruler was placed along the longest side of the board and was used to scale each image. The resolution of the images depends on the size and resolution of the camera sensor, the focal length and the distance between the lens and the object. The data presented here were taken standing at a distance of about 1.0 m from the board, the camera used has a 12.3 MP sensor and the resulting images have an average resolution of 0.26 mm/px. The total number of pebbles present in the sample is 1696. The minimum size of the particles collected was chosen following the criteria recommended by Roussillon et al. (2009): in order to achieve accurate shape values, for a given image resolution, each particle perimeter should be composed of at least 150 pixels. The minimum dimensions considered were therefore about 20 mm and 12 mm for the maximum and intermediate size, respectively.

In order to assess the relative importance of the toolbox used for shape parameters estimation, we created a set of eight black and white images using Adobe Illustrator CC, for which we could compute shape descriptors analytically. These will be further referred to as 'analytical shapes'. Examples and details regarding the analytical shapes can be found in the supporting information. Table 1 summarises the ranges of values used for shape descriptors of analytical shapes (Equations 9–11).

2.5 | Model calibration

The probabilistic nature of the model implies the definition of boundaries for the random selection of the parameters used. The quality of the model's result depends on these boundaries. The model was calibrated to identify the optimal ranges of C_l, C_h and σ_C. The space of possible values considered during the calibration is reported in Table 2.

In order to calibrate the values of the model's parameter and to assess its accuracy, the outline of each pebble manually obtained using the 'Quick Selection tool' available in Adobe Photoshop CC was chosen as the ground truth (GT). The use of this tool requires, especially in the case of shadows, the manual refinement of the segmentation by the operator and might therefore be time consuming and subject to operator bias. The model's parameters have been calibrated using five pebbles that have been selected because they differ in shape, colour, texture and intensity of the shadow. The outlines resulting from the application of our model with each combination of the calibration parameters have been processed using the toolboxes developed by Roussillon et al. (2009) and Zheng and Hryciw (2015) for the estimation of shape parameters. Both toolboxes have been used to process the outlines obtained from the segmentation with Adobe Photoshop CC. We used as an accuracy metric the mean absolute relative error (ε) of three common shape descriptors: elongation, circularity and roundness. The definitions of these three shape descriptors are as follows:

$$e = \frac{I}{L} \tag{9}$$
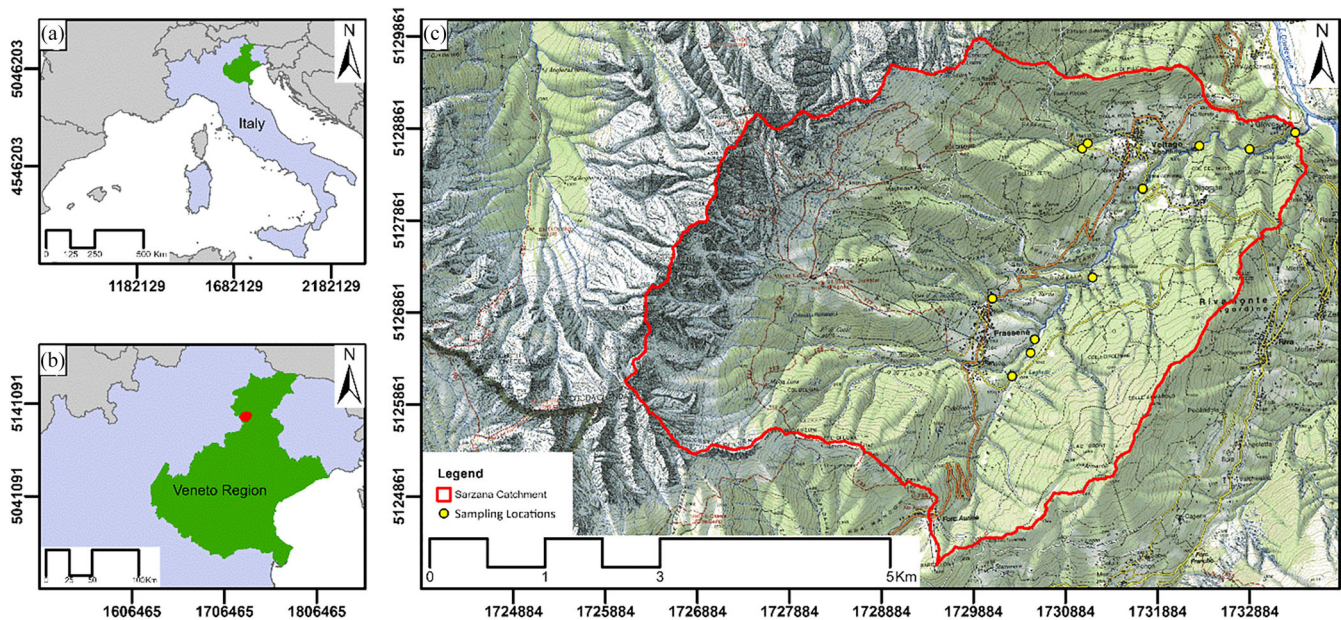
$$C = \frac{4\pi A}{P^2} \tag{10}$$

FIGURE 5 Location of the Sarzana River basin and of the locations where the sediment images used in this study have been collected.

TABLE 1 Overview of shape descriptor values for analytical shapes.

Parameter	Lower limit	Upper limit
e	0.18	0.74
C	0.44	0.97
R_W	0.29	1.00

TABLE 2 Range tested for calibration parameters.

Parameter	Lower limit	Upper limit
C_l	0.0	1.0
C_h	0.0	1.0
σ_C	0.2	5.0

$$R_W = \frac{\frac{1}{N_c}\sum_{i=1}^{N_c} r_i}{R} \tag{11}$$

Where elongation e is the ratio of the intermediate to the longest dimension of the 2D contour (I and L, respectively), A and P are the area and the perimeter of the 2D contour, respectively, and R_W is the roundness according to Wadell (1932). This is defined as the ratio between the average radius of curvature (r_i) of the N_c corners of the 2D contour and the radius of the biggest inscribed circle (R). The relative error (ε) for each descriptor is defined as follows (Equation 12):

$$\varepsilon = \frac{1}{N_p}\sum_{i=1}^{N_p}\frac{|\beta_{GTi} - \beta_{PCi}|}{\beta_{GTi}} \tag{12}$$

where N_p is the number of pebbles in the sample ($N_p = 5$ for the calibration phase), β_{GTi} is the value of a generic shape descriptor obtained using the GT outline for the ith pebble, whereas β_{PCi} is the value of the same shape descriptor obtained using the outline produced by

TABLE 3 Values of model parameters after calibration.

Parameter	Lower limit	Upper limit
C_l	0.1	0.2
C_h	0.0	0.3
σ_C	0.2	5.0

the Probabilistic Canny segmentation method for the same pebble. This metric was chosen because it does not allow compensation of positive and negative relative errors. We also assessed the general performances of the model using an overall error metric defined by equation 13.

$$E = \sqrt{\varepsilon_e^2 + \varepsilon_C^2 + \varepsilon_{R_W}^2} \tag{13}$$

where ε_e is the relative error for pebbles' elongation, ε_C is the relative error for pebbles' circularity and ε_{R_W} is the relative error for pebbles' roundness, as defined earlier.

The combination of parameters selected for the calibration was the one that produced the minimum of the objective function (Ω) defined as the square root of the sum, over all five pebbles, of the squares of the overall error metric (Equation 14).

$$\Omega = \sqrt{\sum_{i=1}^{5} E_i^2} \tag{14}$$

The combination of values corresponding to the minimum of the objective function is provided in Table 3. The parameters were tested between the lower and upper limit in Table 2 with an equidistance of 0.01. The size of the search window around each endpoint was kept constant and equal to 17 pixels. The calibrated model was then applied to the full dataset of images taken in the Sarzana River basin, Italy, as described in Section 2.4.

The relative importance of the segmentation method and of the computational geometry tool for the overall accuracy of the shape values estimation was also assessed. For a given shape descriptor β, the bias of the toolbox by Zheng and Hryciw (2015) was assessed with respect to the one by Roussillon et al. (2009); the average absolute relative difference between the values produced was used $\varepsilon_{Z-R\beta}$ (Equation 15). We used three datasets: the GT outlines, the outlines produced by the Probabilistic Canny segmentation model and the analytical shapes.

$$\varepsilon_{Z-R\beta} = \frac{1}{N_p} \sum_{i=1}^{N_p} \frac{|\beta_{Ri} - \beta_{Zi}|}{\beta_{Ri}} \tag{15}$$

where N_p is the number of pebbles in the dataset, β_{Ri} is the value of the shape descriptor estimated using the toolbox by Roussillon et al. (2009) for the ith pebble and β_{Zi} is the associated value estimated using the toolbox by Zheng and Hryciw (2015).

TABLE 5 Bias of the toolbox by Zheng and Hryciw (2015) with respect to the one by Roussillon et al. (2009) for elongation, circularity and roundness.

Bias	Ground truth	Prob. Canny	Analytical shapes
ε_{Z-Re}	3.5%	3.7%	52.2%
ε_{Z-RC}	7.2%	7.4%	6.0%
ε_{Z-RRw}	14.1%	12.9%	2.6%

TABLE 6 Error of the toolbox by Zheng and Hryciw (2015) and by Roussillon et al. (2009) with respect to analytical shapes for elongation, circularity and roundness.

Error	Zheng et al.	Roussillon et al.
ε_e	3.7%	38.2%
ε_C	3.9%	18.4%
ε_{Rw}	8.9%	15.8%

3 | RESULTS

Out of the 1696 pebbles present in the sample, 1541 passed the visual inspection, meaning that the outline produced by the model appeared to be perfectly matching the actual pebble outline. In terms of visual inspection, therefore the model allowed the accurate segmentation of around 91% of the sample. To quantitatively assess its performance, the outline of all pebbles that passed the visual inspection was also processed using the toolboxes developed by Roussillon et al. (2009) and Zheng and Hryciw (2015). The same toolboxes were also used to analyse the outline of GT pebbles. Table 4 summarises the performances of the proposed segmentation model compared to GT for each shape descriptor and for both toolboxes.

Roundness is the parameter that showed the highest relative error, irrespective of the toolbox used for the estimation of shape parameters. Results for elongation and circularity showed instead good agreement with GT values. Table 5 provides the values of the bias of the toolbox by Zheng and Hryciw (2015) with respect to the one by Roussillon et al. (2009) for elongation, circularity and roundness.

Although the size of the sample is limited to eight shapes, the comparison of the outputs of each toolbox with analytically computed shaper descriptors suggests that the toolbox developed by Zheng and Hryciw (2015) is more accurate than the one by Roussillon et al. (2009) (see Table 6).

Figure 6 provides a visual summary of these results: subplots (a), (c) and (e) compare the two toolboxes for shape descriptors estimation considered in this study, whereas subplots (b), (d) and (f) compare our Probabilistic Canny segmentation method with GT: the 'Quick

selection tool' of Adobe Photoshop CC. In these plots, it is possible once more to observe that, within the limits of our experiment, the choice of a certain toolbox for shape descriptors estimation had a much higher impact on the overall accuracy than the segmentation method used. These plots are also coherent with the comparison of results reported in Tables 4 and 5.

The time required to process an image with several pebbles depends on the number of pebbles and the available computing power. As a reference, in the experiments presented in this manuscript, using 16 GB RAM and 4 cores, 1.8 GHz CPU, an image with 39 pebbles was processed in around 12 min, including the time needed to visually assess the quality of the segmentation of each pebble.

4 | DISCUSSION

The accuracy of the Probabilistic Canny segmentation method presented varies depending on the specific shape parameter used to assess it. In particular, the accuracy in terms of elongation results to be the highest, with lower values for circularity and even lower for roundness. This result provides quantitative evidence for the intuitive argument that the impact of the segmentation method on the shape estimation accuracy increases with increasing detail required to compute the shape descriptor itself.

The comparison of the results reported in Table 4 and Table 5 suggests that the bias associated with the selection of one of the two computational geometry toolboxes is larger than the error introduced by the use of the proposed Probabilistic Canny segmentation method instead of the 'Quick selection tool'.

TABLE 4 Model results in terms of mean absolute error (**E**), standard deviation of the absolute error (σ) and mean absolute relative error (ε) for elongation (**e**), circularity (**C**) and roundness according to Wadell (**Rw**).

Model	E_e	σ_{E_e}	ε_e	E_C	σ_{E_C}	ε_C	E_{Rw}	$\sigma_{E_{Rw}}$	ε_{Rw}
Zheng	0.006	0.021	0.9%	0.013	0.025	1.5%	0.044	0.038	7.5%
Roussillon	0.010	0.025	1.0%	0.007	0.015	0.7%	0.028	0.029	4.3%

FIGURE 6 (a, c, e) Scatterplots representing the bias of the toolbox by Zheng and Hryciw (2015) with respect to the one by Roussillon et al. (2009) for elongation, circularity and roundness, respectively. The legend is consistent for all plots. (b, d, f) Scatterplots provide a visual assessment of the error between our segmentation model and ground truth outlines, obtained with manual segmentation (see Section 2.5). The legend is consistent for all plots.
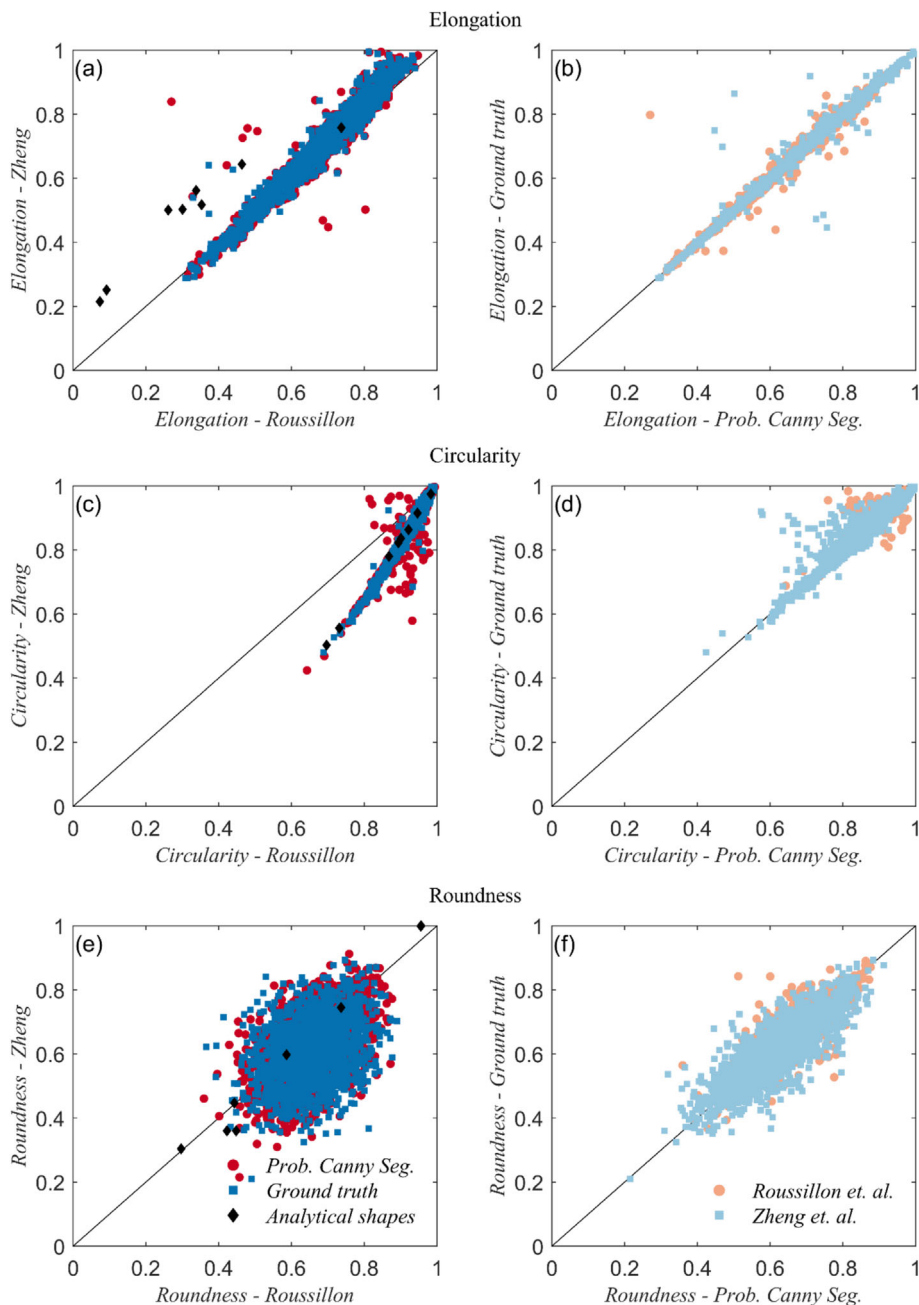
In practical terms, these results can be relevant for studies aiming at correlating sediment morphometry with attrition rates and/or transport, entrainment and deposition conditions. They suggest that, when choosing which parameters to measure, the assessment of the measurement error should account for both the segmentation method and computational geometry tool used because their impact might be of comparable importance. In particular, both factors seem to become increasingly important with the increase in the detail required to compute a given shape property.

The proposed method is completely implemented in MATLAB™ and it can be coupled with the computational geometry toolbox developed by Zheng & Hryciw, 2015. Given its complete automation, the method, therefore, allows results to be reproducible. At the same time, the method allows the user to visually check the quality of the segmentation and to discard pebbles that cannot be correctly segmented. This set-up provides a time-efficient workflow

since it removes the need to double-check the correctness of pebbles segmentation at the end of the process.

5 | CONCLUSIONS AND RECOMMENDATIONS

This paper presents a new method for the automatic segmentation of pebbles outlines from images collected during field surveys. The proposed model is applicable in a range of shadows and contrast conditions and, although the background board used had a similar hue to some of the pebbles, the model accurately segmented their outline. In terms of accuracy, the outlines produced were, in 91% of the examined cases, indistinguishable from true pebble outlines. Moreover, when compared against the herein-defined ground truth, the method showed a comparable accuracy. There is, however, a bias between

different computational geometry toolboxes which in certain cases can be higher than the error between the proposed segmentation method and the ground truth. As a result, when comparing sediment shape properties across environments or through time, the effects of both the segmentation method and the geometry description toolbox need to be taken into consideration, possibly through calibration and validation.

In terms of limitations, strong shadows or intergranular colour or texture changes might limit the ability of the model to accurately segment pebble outlines. In this case, the highest probability edge often occurs along the spurious interface between the background board and the shadow or within the pebble, decreasing the accuracy of automatic segmentation methods. For this dataset, only 9% of the sample presented the aforementioned limitation.

Future research might consider investigating whether the object shape properties fall within acceptable ranges and possible ways to decrease the probability of the edges responsible for such out-of-range values. This approach needs to be tested and verified against visual assessment.

ACKNOWLEDGEMENTS

CONFLICT OF INTERESTS

The authors declare that they have no known competing financial interests or personal relationships that could have appeared to influence the work reported in this paper. The raw images used in this study are available from the corresponding author (a.cattapan@tudelft.nl), upon reasonable request.

ORCID

Alessandro Cattapan 🄳 https://orcid.org/0000-0002-3610-7892
Mário J. Franca 🄳 https://orcid.org/0000-0002-0265-8581

REFERENCES

Adams, J. (1979) Gravel size analysis from photographs. *Journal of the Hydraulics Division*, 105(10), 1247–1255. Available from: https://doi.org/10.1061/JYCEAJ.0005283

Al-Najdawi, N., Bez, H.E., Singhai, J. & Edirisinghe, E.A. (2012) A survey of cast shadow detection algorithms. *Pattern Recognition Letters*, 33(6), 752–764. Available from: https://doi.org/10.1016/j.patrec.2011.12.013

Attal, M. & Lavé, J. (2009) Pebble abrasion during fluvial transport: experimental results and implications for the evolution of the sediment load along rivers. *Journal of Geophysical Research: Earth Surface*, 114(F4), F04023. Available from: https://doi.org/10.1029/2009JF001328

Bradley, W.C. (1970) Effect of weathering on abrasion of granitic gravel, Colorado River (Texas). *Geological Society of America Bulletin*, 81(1), 61. Available from: https://doi.org/10.1130/0016-7606(1970)81[61:EOWOAO]2.0.CO;2

Bradley, W.C., Fahnestock, R.K. & Rowekamp, E.T. (1972) Coarse sediment transport by flood flows on Knik River, Alaska. *GSA Bulletin*, 83(5), 1261–1284. Available from: https://doi.org/10.1130/0016-7606(1972)83[B1261:CSTBFF]2.0.CO;2

Brenna, A. & Surian, N. (2023) Coarse sediment mobility and fluxes in wide mountain streams: insights using the virtual velocity approach. *Geomorphology*, 427, 108625. Available from: https://doi.org/10.1016/j.geomorph.2023.108625

Brewer, P., Leeks, G., & Lewin, J. 1992. Direct measurement of in-channel abrasion processes. Proceedings of the Oslo Symposium, IAHS Pubi. no. 210, 1992.

Buscombe, D., Rubin, D.M. & Warrick, J.A. (2010) A universal approximation of grain size from images of noncohesive sediment. *Journal of Geophysical Research: Earth Surface*, 115(F2), F02015. Available from: https://doi.org/10.1029/2009JF001477

Butler, J.B., Lane, S.N. & Chandler, J.H. (2001) Automated extraction of grain-size data from gravel surfaces using digital image processing. *Journal of Hydraulic Research*, 39(5), 519–529. Available from: https://doi.org/10.1080/00221686.2001.9628276

Canny, J. (1986) A computational approach to edge detection. *IEEE Transactions on Pattern Analysis and Machine Intelligence*, 8(6), 679–698. Available from: https://doi.org/10.1109/TPAMI.1986.4767851

Carbonneau, P.E., Bizzi, S. & Marchetti, G. (2018) Robotic photosieving from low-cost multirotor sUAS: a proof-of-concept: robotic photosieving. *Earth Surface Processes and Landforms*, 43(5), 1160–1166. Available from: https://doi.org/10.1002/esp.4298

Carbonneau, P.E., Lane, S.N. & Bergeron, N.E. (2004) Catchment-scale mapping of surface grain size in gravel bed rivers using airborne digital imagery. *Water Resources Research*, 40(7), W07202. Available from: https://doi.org/10.1029/2003WR002759

Cassel, M., Dépret, T. & Piégay, H. (2017) Assessment of a new solution for tracking pebbles in rivers based on active RFID. *Earth Surface Processes and Landforms*, 42(13), 1938–1951. Available from: https://doi.org/10.1002/esp.4152

Cassel, M., Lavé, J., Recking, A., Malavoi, J.-R. & Piégay, H. (2021) Bedload transport in rivers, size matters but so does shape. *Scientific Reports*, 11(1), 508. Available from: https://doi.org/10.1038/s41598-020-79930-7

Cassel, M., Piégay, H. & Lavé, J. (2017) Effects of transport and insertion of radio frequency identification (RFID) transponders on resistance and shape of natural and synthetic pebbles: applications for riverine and coastal bedload tracking: transport and Rfid-insertion effects on the fragility of pebbles. *Earth Surface Processes and Landforms*, 42(3), 399–413. Available from: https://doi.org/10.1002/esp.3989

Cassel, M., Piégay, H., Lavé, J., Vaudor, L., Hadmoko Sri, D., Wibiwo Budi, S., et al. (2018) Evaluating a 2D image-based computerized approach for measuring riverine pebble roundness. *Geomorphology*, 311, 143–157. Available from: https://doi.org/10.1016/j.geomorph.2018.03.020

Chang, F.-J. & Chung, C.-H. (2012) Estimation of riverbed grain-size distribution using image-processing techniques. *Journal of Hydrology*, 440, 102–112. Available from: https://doi.org/10.1016/j.jhydrol.2012.03.032

Dawson, M. (1988) Sediment size variation in a braided reach of the Sunwapta River, Alberta, Canada. *Earth Surface Processes and Landforms*, 13(7), 599–618. Available from: https://doi.org/10.1002/esp.3290130705

Deal, E., Venditti, J.G., Benavides, S.J., Bradley, R., Zhang, Q., Kamrin, K., et al. (2023) Grain shape effects in bed load sediment transport. *Nature*, 613, 7943. Available from: https://doi.org/10.1038/s41586-022-05564-6

Detert, M. & Weitbrecht, V. (2012) Automatic object detection to analyze the geometry of gravel grains – a free stand-alone tool. In: Colegio de Ingenieros Civiles de Costa Rica. (Ed.) *Proceedings of the international conference on fluvial hydraulics*. San José, Costa Rica: CRC Press.

Ecins, A., Fermüller, C., & Aloimonos, Y. 2014. Shadow free segmentation in still images using local density measure. 2014 IEEE International Conference on Computational Photography (ICCP), 1–8.https://doi.org/10.1109/ICCPHOT.2014.6831803

Engelund, F., & Hansen, E. 1967. A monograph on sediment transport in alluvial streams. Technical University of Denmark 0stervoldgade 10, Copenhagen K.

Ferguson, R., Hoey, T., Wathen, S. & Werritty, A. (1996) Field evidence for rapid downstream fining of river gravels through selective transport. *Geology*, 24(2), 179–182. Available from: https://doi.org/10.1130/0091-7613(1996)024<0179:FEFRDF>2.3.CO;2

Gonzalez, R.C., Woods, R.E. & Eddins, S.L. (2009) *Digital image processing using MATLAB*, (2nd ed). Gatesmark Pub.

Hayakawa, Y. & Oguchi, T. (2005) Evaluation of gravel sphericity and roundness based on surface-area measurement with a laser scanner. *Computers & Geosciences*, 31(6), 735–741. Available from: https://doi.org/10.1016/j.cageo.2005.01.004

Hodge, R., Brasington, J. & Richards, K. (2009) In situ characterization of grain-scale fluvial morphology using terrestrial laser scanning. *Earth Surface Processes and Landforms*, 34(7), 954–968. Available from: https://doi.org/10.1002/esp.1780

Huang, G.-H., Atkinson, P.M. & Wang, C.-K. (2018) Quantifying the scales of spatial variation in gravel beds using terrestrial and airborne laser scanning data. *Open Geoscience*, 10(1), 607–617. Available from: https://doi.org/10.1515/geo-2018-0048

Jones, L.S. & Humphrey, N.F. (1997) Weathering-controlled abrasion in a coarse-grained, meandering reach of the Rio Grande: implications for the rock record. *GSA Bulletin*, 109(9), 1080–1088. Available from: https://doi.org/10.1130/0016-7606(1997)109<1080:WCAIAC>2.3.CO;2

Kodama, Y. (1994) Experimental study of abrasion and its role in producing downstream fining in gravel-bed rivers. *Journal of Sedimentary Research*, 64(1a), 76–85. Available from: https://doi.org/10.2110/jsr.64.76

Koh, T. K., Miles, N., Morgan, S., & Hayes-Gill, B. 2007. Image Segmentation of Overlapping Particles in Automatic Size Analysis Using Multi-Flash Imaging. 2007 IEEE Workshop on Applications of Computer Vision (WACV'07), 47. https://doi.org/10.1109/WACV.2007.37

Krumbein, W.C. (1941) The effects of abrasion on the size, shape and roundness of rock fragments. *The Journal of Geology*, 49(5), 482–520. Available from: https://doi.org/10.1086/624985

Langhammer, J., Lendzioch, T., Miřijovský, J. & Hartvich, F. (2017) UAV-based optical Granulometry as tool for detecting changes in structure of flood depositions. *Remote Sensing*, 9(3), 240. Available from: https://doi.org/10.3390/rs9030240

Le, H., & Samaras, D. 2020. From Shadow Segmentation to Shadow Removal. arXiv:2008.00267 [Cs]. http://arxiv.org/abs/2008.00267

Lewin, J. & Brewer, P.A. (2002) Laboratory simulation of clast abrasion. *Earth Surface Processes and Landforms*, 27(2), 145–164. Available from: https://doi.org/10.1002/esp.306

McCallister, W. O., & Hung, C.-C. 2003. Image segmentation using dynamic run-length coding technique. Proceedings of the 13th Scandinavian Conference on Image Analysis, 343–348.

Meyer-Peter, E., & Müller, R. 1948. Formulas for bed-load transport. Rep. 2nd Meet. Int. Assoc. Hydraul. Struct. Res, 39–64.

Montenegro Ríos, A., Sarocchi, D., Nahmad-Molinari, Y. & Borselli, L. (2013) Form from projected shadow (FFPS): an algorithm for 3D shape analysis of sedimentary particles. *Computers & Geosciences*, 60, 98–108. Available from: https://doi.org/10.1016/j.cageo.2013.07.008

Rickenmann, D. (2017) Bed-load transport measurements with geophones and other passive acoustic methods. *Journal of Hydraulic Engineering*, 143(6), 03117004. Available from: https://doi.org/10.1061/(ASCE)HY.1943-7900.0001300

Roussillon, T., Piégay, H., Sivignon, I., Tougne, L. & Lavigne, F. (2009) Automatic computation of pebble roundness using digital imagery and discrete geometry. *Computers & Geosciences*, 35(10), 1992–2000. Available from: https://doi.org/10.1016/j.cageo.2009.01.013

Schneider, J.M., Rickenmann, D., Turowski, J.M., Schmid, B. & Kirchner, J.W. (2016) Bed load transport in a very steep mountain stream (Riedbach, Switzerland): measurement and prediction. *Water Resources Research*, 52(12), 9522–9541. Available from: https://doi.org/10.1002/2016WR019308

Schumm, S.A. & Stevens, M.A. (1973) Abrasion in place: a mechanism for rounding and size reduction of coarse sediments in Rivers. *Geology*, 1(1), 37–40. Available from: https://doi.org/10.1130/0091-7613(1973)1<37:AIPAMF>2.0.CO;2

Seal, R. & Paola, C. (1995) Observations of downstream fining on the north fork Toutle River near Mount St. Helens, Washington. *Water Resources Research*, 31(5), 1409–1419. Available from: https://doi.org/10.1029/94WR02976

Sobel, I. 2014. An Isotropic 3x3 Image Gradient Operator. Presentation at Stanford A.I. Project 1968.

Sun, Q., Zheng, J. & Li, C. (2019) Improved watershed analysis for segmenting contacting particles of coarse granular soils in volumetric images. *Powder Technology*, 356, 295–303. Available from: https://doi.org/10.1016/j.powtec.2019.08.028

Tunwal, M., Mulchrone, K.F. & Meere, P.A. (2020) Image based particle shape analysis toolbox (IPSAT). *Computers & Geosciences*, 135, 104391. Available from: https://doi.org/10.1016/j.cageo.2019.104391

van Rijn, L.C. (1984) Sediment transport, part I: bed load transport. *Journal of Hydraulic Engineering*, 110(10), 1431–1456. Available from: https://doi.org/10.1061/(ASCE)0733-9429(1984)110:10(1431)

Vangla, P., Roy, N. & Gali, M.L. (2017) Image based shape characterization of granular materials and its effect on kinematics of particle motion. *Granular Matter*, 20(1), 6. Available from: https://doi.org/10.1007/s10035-017-0776-8

Wadell, H. (1932) Volume, shape, and roundness of rock particles. *The Journal of Geology*, 40(5), 443–451. Available from: https://doi.org/10.1086/623964

Wang, Y., Liang, X., Flener, C., Kukko, A., Kaartinen, H., Kurkela, M., et al. (2013) 3D modeling of coarse fluvial sediments based on mobile laser scanning data. *Remote Sensing*, 5(9), 4571–4592. Available from: https://doi.org/10.3390/rs5094571

Warrick, J.A., Rubin, D.M., Ruggiero, P., Harney, J.N., Draut, A.E. & Buscombe, D. (2009) Cobble cam: grain-size measurements of sand to boulder from digital photographs and autocorrelation analyses. *Earth Surface Processes and Landforms*, 34(13), 1811–1821. Available from: https://doi.org/10.1002/esp.1877

Wentworth, C.K. (1919) A laboratory and field study of cobble abrasion. *The Journal of Geology*, 27(7), 507–521. Available from: https://doi.org/10.1086/622676

Woodget, A.S. & Austrums, R. (2017) Subaerial gravel size measurement using topographic data derived from a UAV-SfM approach. *Earth Surface Processes and Landforms*, 42(9), 1434–1443. Available from: https://doi.org/10.1002/esp.4139

Wyss, C.R., Rickenmann, D., Fritschi, B., Turowski, J.M., Weitbrecht, V. & Boes, R.M. (2016) Measuring bed load transport rates by grain-size fraction using the Swiss plate geophone signal at the Erlenbach. *Journal of Hydraulic Engineering*, 142(5), 04016003. Available from: https://doi.org/10.1061/(ASCE)HY.1943-7900.0001090

Zheng, J. & Hryciw, R.D. (2015) Traditional soil particle sphericity, roundness and surface roughness by computational geometry. *Géotechnique*, 65(6), 494–506. Available from: https://doi.org/10.1680/geot.14.P.192

Zheng, J. & Hryciw, R.D. (2016) Segmentation of contacting soil particles in images by modified watershed analysis. *Computers and Geotechnics*, 73, 142–152. Available from: https://doi.org/10.1016/j.compgeo.2015.11.025

SUPPORTING INFORMATION

Additional supporting information can be found online in the Supporting Information section at the end of this article.

How to cite this article: Cattapan, A., Gurini, A., Paron, P., Ballio, F. & Franca, M.J. (2024) A method for segmentation of pebble images in the presence of shadows. *Earth Surface Processes and Landforms*, 1–11. Available from: https://doi.org/10.1002/esp.6027